RESEARCH ARTICLE

Check for updates

Surface defect engineering of mesoporous Cu/ZnS nanocrystal-linked networks for improved visible-light photocatalytic hydrogen production†

Ioannis Daskalakis,[a] Ioannis Vamvasakis,[a] Ioannis T. Papadas,[b] Sotirios Tsatsos,[c] Stelios A. Choulis, [ID][b] Stella Kennou[c] and Gerasimos S. Armatas [ID] *[a]

Transition metal sulfides have been emerging as one of the most attractive and prospective catalysts for the direct conversion of solar energy into chemical fuels. Their intriguing compositional and electronic characteristics and their feasibility for integration in porous architectures endow metal sulfide materials with superior activity for photochemical catalysis. In the present work, high-surface-area Cu-doped ZnS nanocrystal (NC)-linked mesoporous frameworks are successfully synthesized for use as cost-effective catalysts for photochemical hydrogen evolution. Benefiting from the suitable band-edge alignment and enhanced visible light absorption resulting from the interfacial charge transfer between ZnS and Cu$_2$S NCs, there is a spatial separation of charge carriers which leads to excellent activity for photocatalytic hydrogen production. Moreover, the results obtained here show that surface defect passivation through a wet-chemical sulfidation process effectively increases the photochemical performance of the composite catalysts by improving the transport efficiency of electrons at the Cu$_2$S/ZnS interface and changing the Helmholtz layer potential drop at the ZnS/Cu$_2$S/electrolyte junction. Thus, a remarkable improvement of 1 mmol h^{-1} g$_{cat}$$^{-1}$ for hydrogen evolution is observed with the sulfide-treated Cu$_2$S/ZnS catalyst containing 5 mol% Cu, which is associated with a 17.6% apparent quantum yield under 410 nm irradiation. This work provides an interesting strategy for enhancing the interface charge transfer properties and hydrogen evolution activity of metal sulfides by surface defect engineering with sulfide ions.

1. Introduction

Currently, compared to unsustainable hydrocarbon fuels and high-energy consumption solutions (such as steam methane reforming and water electrolysis),[1] solar light hydrogen generation has been regarded as one of the most promising methods for clean, economical, and environmentally friendly production of fuels.[2] In solar-to-fuel conversion technology, semiconductor materials, like TiO$_2$, NiO$_x$, Ta$_3$N$_5$, CdS, and ZnS, and crystalline metal chalcogenide compounds, like (CH$_3$NH$_3$)$_2$Ag$_4$Sn$_3$S$_8$, (NH$_4$)AgSb$_2$S$_4$, Mn$_2$Sb$_2$S$_5$(N$_2$H$_4$)$_3$, and ((CH$_3$)$_2$NH$_2$)$_2$In$_2$Sb$_2$S$_{7-x}$Se$_x$, have a key function.[3] They act as

sensitizers for light-initiated redox reactions due to the appropriate electronic structure that absorbs light and produces photoexcited electron–hole pairs. The width of the bandgap (E_g) and appropriate matching of conduction band (CB) and valence band (VB) levels greatly affect the ability of these materials to photocatalytically split water into hydrogen – the energy band positions should be sufficient to ensure visible-light absorption (it represents more than 40% of the solar energy) and bring about water reduction (the CB potential must be located above the H$^+$/H$_2$ redox potential, *i.e.* −0.41 V *vs.* NHE at pH 7).[4] Moreover, the high conductivity of charge carriers, fast surface reaction kinetics and cost effectiveness are also key requirements for the photocatalytic activity of the semiconducting materials.

Recently, II–VI compound semiconductors, especially zinc sulfide and selenide (ZnS/Se), have drawn intensive attention in energy-storage and photochemical devices, such as Li-ion batteries,[5] solar cells[6] and light-induced photocatalysts.[7] Their main advantages are the tunability of electronic structures, high intrinsic electrical conductivity, rich redox activity, and strong reduction ability of photoinduced electrons for hydrogen evolution.[8] Nevertheless, ZnS-based photocatalysts, such

[a]Department of Materials Science and Technology, University of Crete, Heraklion 70013, Greece. E-mail: garmatas@materials.uoc.gr
[b]Molecular Electronics and Photonics Research Unit, Department of Mechanical Engineering and Materials Science and Engineering, Cyprus University of Technology, Limassol 3041, Cyprus
[c]Department of Chemical Engineering, Surface Science Laboratory, University of Patras, Patra 26504, Greece
†Electronic supplementary information (ESI) available: EDS and EIS results, N$_2$ physisorption isotherms, catalytic data, XRD patterns, and XPS and PL spectra of ZS, CZS-*n* and CZS′-5 NCAs. See DOI: 10.1039/d0qi01013h

This journal is © the Partner Organisations 2020

Inorg. Chem. Front., 2020, **7**, 4687–4700 | **4687**

as S-defective ZnS microspheres[9] and ZnS microparticles,[10] usually suffer from limited solar light absorption and/or poor electron–hole separation yield, which severely impede their viable applications. To overcome these limitations and enhance the visible-light photocatalysis of ZnS, recently, various strategies such as synthesis of solid solutions (*e.g.*, $Zn_{1-x}Cu_xS$ and $(AgIn)_xZn_{2(1-x)}S_2$),[11] construction of heterojunctions (*e.g.*, Au-decorated ZnS and Ru-loaded ZnS),[12] and optimization of the morphology (*e.g.*, fabrication of 3D ZnS nanoarchitectures)[13] have been employed in the synthesis of ZnS-based photocatalysts. Among them, construction of heterojunctions (electronic contacts) between ZnS and a narrow bandgap semiconductor provides one of the most efficient ways to realize high photochemical performance. ZnS-based heterostructures have been proved as efficient catalysts for chemical energy conversion due to the band bending at the junction interface, which provides effective transfer and separation of the photogenerated charge carriers.[14] Furthermore, the multi-componential nature of these materials can enhance the overall catalytic efficiency due to the spatial separation of reduction and oxidation active sites on the surface of different components – the excited electrons can participate in reduction reactions on one surface while the holes can be consumed by the oxidation reaction at a separate surface. Therefore, the rational design of nanocomposite catalysts with desired morphologies and appropriate electronic band structures is critically important to achieve a more stable and enhanced photocatalytic performance.

In this work, high-surface-area mesoporous networks of Cu-doped ZnS nanocrystals (NCs) were synthesized and investigated as photocatalysts for visible light irradiated ($\lambda \geq 420$ nm) reduction of water to hydrogen. Although ZnS is a wide bandgap semiconductor that absorbs only UV light (it has a 3.5–3.9 eV energy gap), Cu^+ doping can extend its visible-light response by introducing tail states (electron donor levels) within the bandgap of ZnS.[15] On the other hand, the Cu^+ dopant will also induce the formation of sulfur vacancies which may act as electron and hole-trapping centers.[16] For this purpose, we systematically study the effect of Cu^+ doping on the electronic band structure and visible-light photochemical activity of the assembled Cu/ZnS NCs. To this end, porous Cu-doped ZnS nanoarchitectures with a large surface area (up to 313 m^2 g^{-1}) and various compositions (the Cu doping level varies from 2 to 10 mol%) were successfully prepared by a two-step chemical process that involves polymer-assisted aggregating assembly of colloidal ZnS NCs, followed by chemical transformation of constituent nanoparticles into Zn–S–Cu composites. Moreover, on a particular composite catalyst, we show that surface defect sites can be passivated to a large extent by a sulfidation process on the NC-linked structure, apparently leading to improved charge transfer at the Cu_2S/ZnS interface and better photocatalytic activity. This finding, which is supported by optical absorption and electrochemical spectroscopic studies, is especially important as it may offer a potential solution to the poor photochemical performance of defective interfacial structures. Las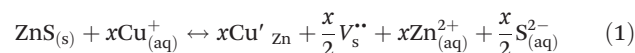tly, a mechanism for visible-light-driven photocatalytic hydrogen evolution in the present system is proposed according to the experimental results.

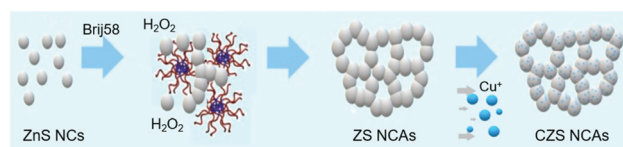## 2. Results and discussion

2.1 Synthesis and morphology of Cu/ZnS NCAs

The synthesis procedure of Cu-doped ZnS NC-assembled structures is illustrated in Scheme 1. Initially, a porous network of ZnS linked NCs (denoted as ZS NCAs) was obtained by a polymer-assisted oxidative aggregating method, in which the colloidal ZnS NCs co-assemble with a block copolymer Brij-58 $(HO(CH_2CH_2O)_{20}C_{16}H_{33})$ into a mesostructured organic/inorganic composite under slow evaporation of the solvent.[17] Next, the organic template was removed by solvent extraction to give a rigid mesoporous network of connected nanoparticles. The porous assemblies of the Cu-doped ZnS NCs (denoted as CZS NCAs) were then converted from the ZnS mesoporous network by an ion-exchange reaction with Cu^+; we used different concentrations of CuCl to produce CZS-*n* heterostructures with various compositions [*n* (mol% Cu) = Cu/(Cu + ZnS) × 100]. The success of this process is visually evident from the color change of the pristine ZS NCAs sample from white-gray to olive-green. In this ion-exchange reaction, the large disparity of the solubility product K_{sp} between ZnS (4.0×10^{-24}) and Cu_2S (2.0×10^{-47}) is the driving force for the incorporation of Cu^+ into the ZnS lattice.[18] The specific advantage of using the ion-exchange method is that it enables the growth of Cu_2S species within the ZnS crystal structure with intimate contact between the two semiconductors (*i.e.*, by the formation of the Cu_2S/ZnS junction). Such a strong interfacial contact is beneficial for improving the photocatalytic properties as it is expected to engender more efficient separation and migration of photogenerated carriers.

The incorporation of Cu^+ ions into the ZnS lattice may lead to the formation of interface defect sites at the ZnS/Cu_2S junction according to eqn (1), in which the exchange of Zn^{2+} with Cu^+ (Cu'_{Zn}) involves the production of S-atom vacancies ($V_s^{\bullet\bullet}$) in the Zn–S–Cu lattice for charge balance.

$$ZnS_{(s)} + xCu^+_{(aq)} \leftrightarrow xCu'_{Zn} + \frac{x}{2}V_s^{\bullet\bullet} + xZn^{2+}_{(aq)} + \frac{x}{2}S^{2-}_{(aq)} \quad (1)$$

Such S-related defect sites can induce the formation of midgap electronic states (deep or shallow trap states), which may serve as trap centers for charge carriers, causing electron–hole pair recombination. Therefore, controlling the quantity of defects in the ZnS lattice is critical in photocatalytic reactions.

Scheme 1 Schematic representation of the synthesis of mesoporous ZnS (ZS) and Cu-doped ZnS (CZS) NC-linked assemblies (NCAs).

4688 | *Inorg. Chem. Front.*, 2020, **7**, 4687–4700

This journal is © the Partner Organisations 2020

To improve the charge transport and catalytic efficiency, we post-treated the CZS-5 sample, which is the most active catalyst in this series, with sulfide (S^{2-}) solution in order to replace missing sulfur atoms in the composite structure. The resultant sulfurated catalyst was denoted as CZS′-5.

Energy-dispersive X-ray spectroscopy (EDS) analysis showed that the CZS heterostructures are composed of Zn, Cu and S elements with different molar ratios, which correspond to a Cu loading from ∼2 to ∼10 mol% (see Table S1†). Of particular note, the Cu content, as determined by EDS analysis, is well consistent with the expected composition from the stoichiometry of reactions. This suggests the complete incorporation of Cu^+ ions into the ZnS lattice.

The morphology and crystal structure of the as-prepared materials were examined by combining X-ray diffraction (XRD) and transmission electron microscopy (TEM). Fig. 1a shows the XRD patterns of the mesoporous ZS and CZS NCAs. All the diffraction peaks can be indexed to the zinc blende structure of ZnS with a lattice parameter $a_0 = 5.41$ Å (space group $F\bar{4}3m$, JCPDS no. 05-0566). The broadening of the X-ray diffraction peaks signifies the small grain composition of the materials; in particular, the average diameter of the crystallites deduced from the peak broadening using the Scherrer equations is about 3 nm. After the sulfidation process, the crystal structure of pristine CZS-5 is well retained, as shown in Fig. 1a. XRD analysis, however, does not provide any insightful information about the presence of copper sulfide (Cu_xS) species, even in the XRD pattern of the 10 mol% Cu-doped sample. This is attributed to the high dispersion of Cu^+ ions in the lattice of ZnS. Nevertheless, our further studies with electron diffraction and X-ray photoelectron spectroscopy confirmed the existence of the Cu_2S phase, indicating that the Cu^+ ions successfully replace the Zn^{2+} ions during the ion-exchange reaction (see below).

Fig. 1b and c display typical TEM images of the as-prepared CZS-5 sample. The images show that small-sized nanoparticles are interconnected with each other to form a network-like structure with high porosity. From the magnified TEM image in Fig. 1c, the size of the constituent nanoparticles is found to be around 5–6 nm, which is close to the size of starting nanoparticles (*ca.* 5 nm).[19] Further analysis by high-resolution TEM (HRTEM) reveals that the assembled structure possesses well-defined lattice fringes throughout the entire nanoparticles with interplanar spacings of 2.7 and 3.1 Å, which can be ascribed to the (200) and (111) planes (along the [011] zone-axis) of cubic ZnS (Fig. 1c, inset), in agreement with XRD results. Moreover, the comparison of the calculated electron diffraction patterns and the experimentally recorded ones demonstrates the presence of the zinc blende structure of ZnS along with the cubic structure (space group $Fm\bar{3}m$) of Cu_2S; in Fig. 1d, the selected area electron diffraction (SAED) pattern shows a series of Debye–Scherrer diffraction rings that could be indexed to the (111), (220), (311) and (422) facets of ZnS (marked with yellow curves) and the (200), (220) and (311) facets of Cu_2S (marked with blue curves). Combined with the XRD patterns, these results clearly indicate that the pore walls consisted of connected cubic zinc blende ZnS and cubic chalcocite Cu_2S NCs. This supports the notion that the transformation of ZnS into Zn–S–Cu is topotactic in nature, that is, the crystal structure of ZnS is preserved after transformation.

X-ray photoelectron spectroscopy (XPS) was employed to investigate the phase composition and chemical nature of the composite Zn–S–Cu framework. Fig. 2 shows the XPS spectra for the pristine and sulfurated CZS-5 samples. All binding energy values in the XPS spectra were calibrated according to the C 1s line at 284.6 eV. The carbon element mainly originates from atmosphere contamination during the handling of the samples. In the CZS-5 material, the Zn $2p_{3/2}$ photoelectron peak appears at a binding energy of 1021.6 ± 0.2 eV (Fig. 2a). However, this position does not allow for an unambiguous identification of Zn(ɪɪ) compounds, since the literature values for Zn $2p_{3/2}$ binding energies are quite similar to ZnS (1021.6 eV) and ZnO (1022.1 eV).[20] For this reason, the Auger α parameter, that is, the binding energy of the Zn $2p_{3/2}$ peak + the kinetic energy of the Zn $L_3M_{45}M_{45}$ Auger peak, was evaluated and used to confirm the presence of ZnS. According to the literature, the Zn Auger parameter value varies from ∼2010.1 to ∼2011.3 eV for ZnS, while the corresponding values range from ∼2009.5 to ∼2010 eV for ZnO.[21] For the CZS-5 NCAs, the Auger parameter is found to be 2010.3 ± 0.2 eV, which probably reflects the existing phase of ZnS (Fig. 2b). The Cu $2p_{3/2}$ core-level signal appears at a binding energy of 932.1 ± 0.2 eV, which can be ascribed to the monovalent copper ions (Fig. 2c), consistent with other reported results.[22] Generally, the
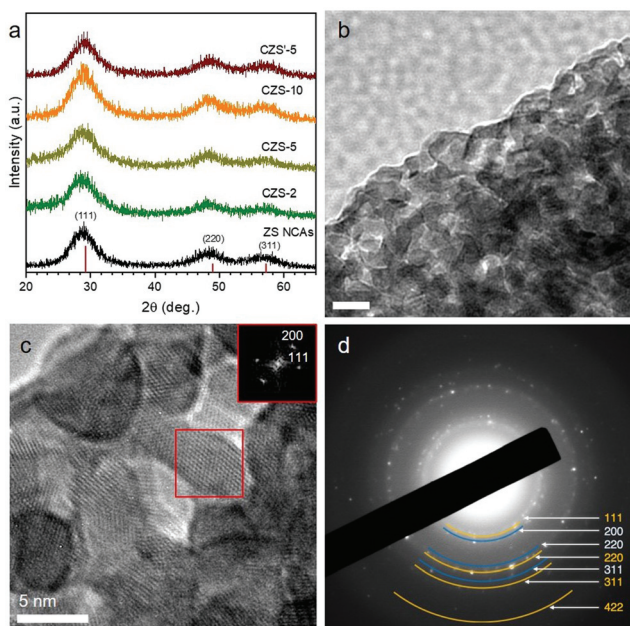

Fig. 1 (a) XRD patterns of the as-synthesized ZS, CZS and CZS′-5 NC assemblies. The XRD lines of cubic ZnS (JCPDS no. 05-0566) are also given. (b) Typical TEM and (c) high-resolution TEM (HRTEM) (inset: the [011] zone-axis FFT pattern recorded from the red square box, showing the (111) and (200) diffractions of zinc blende ZnS) images, and (d) SAED pattern of the CZS-5 mesoporous architecture.
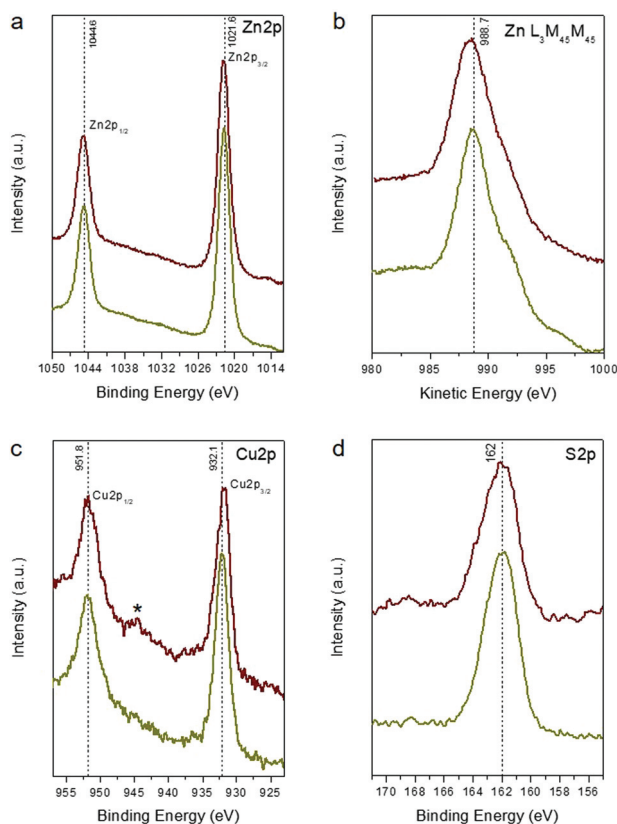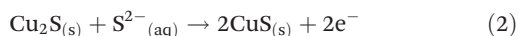
This journal is © the Partner Organisations 2020

Inorg. Chem. Front., 2020, **7**, 4687–4700 | **4689**

Fig. 2 XPS spectra of the (a) Zn 2p, (b) Zn L3M45M45 Auger, (c) Cu 2p and (d) S 2p core-level lines for the mesoporous CZS-5 (dark yellow line) and CZS′-5 (red line) NCAs. In panel (c), the symbol shows the satellite peak at ~944.3 eV characteristic of Cu^{2+} ions.

$2p_{3/2}$ binding energy for the compounds containing Cu^+ (e.g., Cu_2O, Cu_2S) locates at 932.2–932.8 eV,[23] while that for the compounds containing Cu^{2+} ions locates around 933–935 eV,[24] accompanying with a characteristic "shake-up" satellite peak at 940–945 eV. Taken together the SAED analysis, these results are consistent with the presence of Cu_2S species in the ZnS lattice. This is further corroborated by the presence of a single peak in the core-level spectrum of the S 2p region at 162 ± 0.2 eV, which is attributed to the sulfide (S^{2-}) species.

Interestingly, during the sulfidation process, some of the S^{2-} ions are incorporated into the Zn–S–Cu host lattice, causing a partial oxidation of Cu^+ to Cu^{2+} (eqn (2)).

$$Cu_2S_{(s)} + S^{2-}_{(aq)} \rightarrow 2CuS_{(s)} + 2e^- \qquad (2)$$

The presence of paramagnetic Cu^{2+} (probably as CuS and/or surface $Cu(OH)_2$ groups) in the sulfurated sample was confirmed by the Cu 2p XPS spectrum due to the appearance of the weak "shake-up" satellite peak in the higher binding energy range (~944.3 eV), as seen in Fig. 2c.[25] In addition, a small amount of sulfur species at certain higher oxidation states is, however, observed in the surface of CZS′-5, judging from the weak feature at 169 ± 0.2 eV in the S 2p region (Fig. 2d).
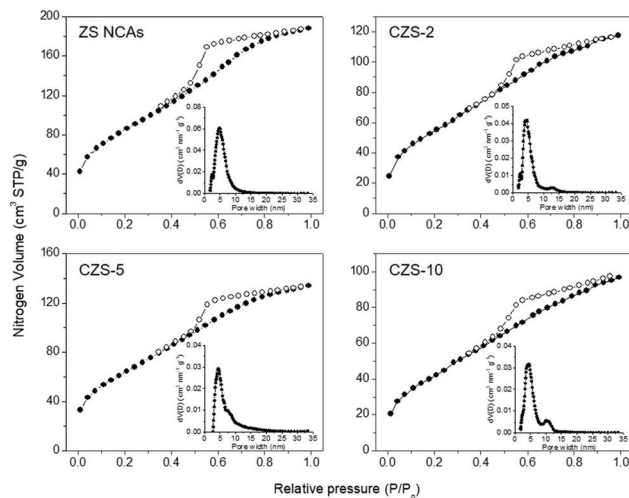

Fig. 3 N_2 adsorption and desorption isotherms at −196 °C and (inset) the corresponding pore-size distribution plots for the mesoporous ZS and CZS NCAs.
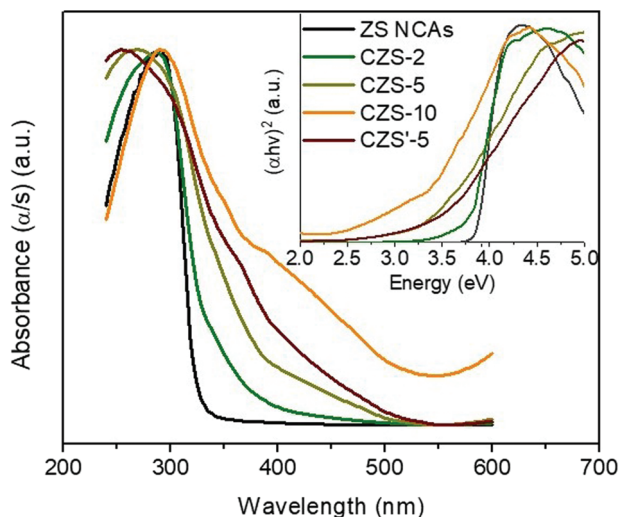
The porosity of the resulting materials was probed with nitrogen physisorption measurements at −196 °C. Fig. 3 and Fig. S1† display the N_2 adsorption and desorption isotherms and the corresponding pore-size distribution plots of the mesoporous ZS, CZS and CZS′-5 NCAs. All the isotherms showed typical type-IV behavior associated with a H_2-type hysteresis loop (according to IUPAC classification) at higher relative pressures, which are characteristic of mesoporous structures with interconnected pores.[26] The mesoporous CZS samples possess a Brunauer–Emmett–Teller (BET) surface area of 150–235 m^2 g^{-1} and a total pore volume of 0.14–0.18 cm^3 g^{-1}, which are slightly lower than those of the pristine ZS material (314 m^2 g^{-1}, 0.28 cm^3 g^{-1}). The decrease in the surface area and pore volume for the Cu-doped samples is presumably due to a partial cleavage of the NC-linked network during the ion-exchange process. Furthermore, the surface area of the sulfurated material becomes lower than that in the untreated sample (yet remains high enough to enable mass transport and diffusion between the nanoparticles), possibly due to an etching-like effect of S^{2-} ions on the nanoparticle-assembled structure.[27] The pore size in these materials was determined from the adsorption branch of isotherms using the non-local density functional theory (NLDFT) model. The results of ZS, CZS and CZS′-5 NCAs reveal a quite narrow pore size distribution with an average size of ~4.4–4.8 nm (insets of Fig. 3 and Fig. S1†). All the textural parameters for the as-prepared materials are given in Table 1.

The well-defined electronic structure of the title materials leads to strong optical absorption in the ultraviolet-visible (UV–vis) spectrum, ranging from ~320 nm for ZS to ~400 nm for the CZS NCAs (Fig. 4), which corresponds to the interband VB-to-CB electron transition. The electronic band structure of these materials is characterized by a large energy gap, which is estimated to be 3.88 eV for pristine ZS and 3.09 to 3.75 eV for the CZS NCAs (Table 1), using the Tauc method for a direct

Table 1 Textural parameters and energy band gap values for mesoporous ZS, CZS and CZS′-5 NCAs
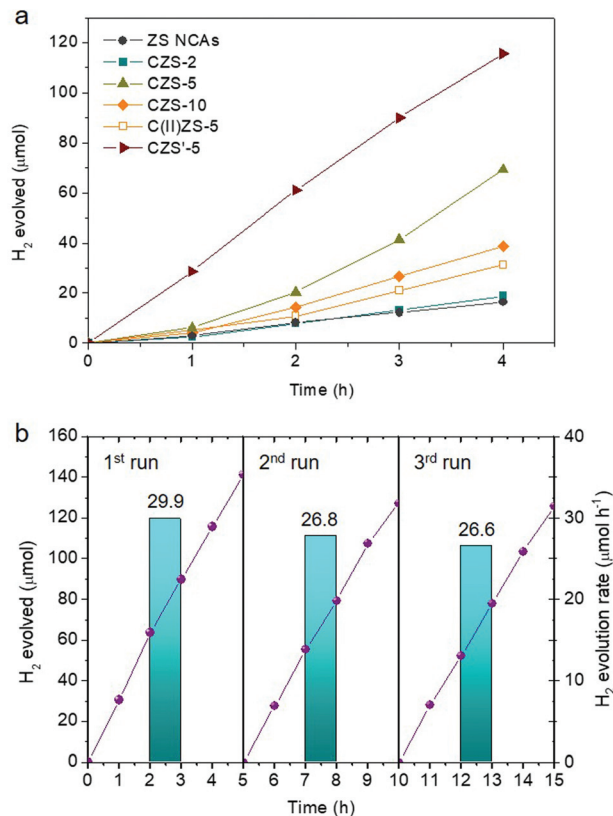
Sample	Surface area ($m^2\ g^{-1}$)	Pore volume ($cm^3\ g^{-1}$)	Pore diameter (nm)	Energy bandgap (eV)
ZS	314	0.28	4.8	3.88
CZS-2	235	0.18	4.5	3.75
CZS-5	205	0.17	4.4	3.32
CZS-10	150	0.14	4.4	3.09
CZS′-5[a]	142	0.15	4.6	3.36

[a] Sulfurated CZS-5 sample.

Fig. 4 UV–vis diffuse reflectance spectra and Tauc plots (inset) for mesoporous ZS, CZS and CZS′-5 NCAs.

Fig. 5 (a) Time courses for photocatalytic H_2 production for mesoporous ZS and various CZS NCAs. The H_2 evolution *versus* time for the Cu^{2+}-doped ZnS (C(II)ZS-5) catalyst is also given. (b) Recycling study of the CZS′-5 catalyst. The H_2 evolution rates were averaged over 5 h of irradiation. All the photocatalytic reactions were performed by suspending 20 mg of the catalyst in 20 mL of water containing 0.25 M Na_2SO_3 and 0.35 M Na_2S, under $\lambda \geq 420$ nm light irradiation.

band gap semiconductor (Fig. 4, inset). The large hypsochromic (blue) shift in the energy gap of mesoporous ZS relative to the bandgap of bulk zinc blende ZnS ($\sim$3.7 eV)[28] is attributed to the quantum confinement in the ZnS nanoparticles due to the very small grain size (*ca.* 5–6 nm according to the TEM observation). Moreover, the decrease in the energy gap with increasing Cu content is attributed to the strong electron interactions between the electronic states in the ZnS and Cu_2S NCs. This indicates that the Cu_2S species are mainly incorporated into the structure of ZnS and do not grow on the ZnS surface. In addition, the incorporation of Cu_2S into the ZnS lattice leads to an increase in the light absorption between 380 and 500 nm, which is helpful for improving the visible-light absorbance and thus the photocatalytic efficiency of the catalyst.

2.2 Photocatalytic hydrogen evolution study

Benefiting from the intriguing electronic properties and mesoporous nanoarchitecture, the CZS assemblies are expected to achieve superior photocatalytic performance. The photocatalytic activity of the resulting materials was studied by visible light irradiated ($\lambda \geq 420$ nm) reduction of water. The photocatalytic experiments were initially carried out in a Pyrex

glass reactor by stirring 20 mL of a Na_2SO_3/Na_2S aqueous solution containing 20 mg of the catalyst. As shown in Fig. 5a, the ZS NCAs show poor photocatalytic hydrogen evolution activity of around 4.1 μmol h^{-1} due to the limited light absorption – it has an energy gap (E_g) of $\sim$3.9 eV. In striking contrast, the Cu^+ doping considerably enhanced the hydrogen evolution activity of ZnS, proving that the Cu_2S clusters realize efficient photocatalytic reactions under visible light. For the CZS composites, the evolution rate of H_2 increases with increasing Cu content and attains a maximum of 17.3 μmol h^{-1} at 5 mol%, which is about 4.2 times higher than that of undoped ZS. Afterward, further increase of the Cu doping level leads to a marked reduction of the photoactivity, as inferred by the lower H_2 evolution rate of the CZS catalyst with 10 mol% Cu content (9.7 μmol h^{-1}). This could be explained by the fact that excessive Cu^+ doping may produce too many defect states (S vacancies) acting as electron–hole recombination centers. We further confirmed the effectiveness of the Cu_2S phase by preparing a 5% Cu^{2+}-doped ZnS (denoted as C(II)ZS-5) catalyst and exploring possible differences with respect to the photocatalytic hydrogen evolution performance of CZS-5; C(II)ZS-5

This journal is © the Partner Organisations 2020

Inorg. Chem. Front., 2020, **7**, 4687–4700 | **4691**

was prepared by a similar impregnation method using $CuCl_2$ as a precursor (see details in the Experimental section). Interestingly, when measured under identical conditions, the hydrogen generation efficiency with C(II)ZS-5 (7.8 μmol h^{-1}) was remarkably lower than that of CZS-5 (Fig. 5a). This demonstrates that Cu_2S nanoparticles have great potential for photocatalytic hydrogen production.

Next, we investigated the optimized performance of the CZS-5 catalyst by measuring the hydrogen evolution with different concentrations of the catalyst and types of sacrificial agents. Control experiments showed that there is an increase of the H_2 evolution rate with increasing catalyst addition until reaching a maximum at 1 g L^{-1} (Fig. S2†). We interpret the dependence of H_2 evolution on the catalyst concentration as an enhancement of light absorption by the catalyst nanoparticles. However, at an excess concentration of the catalyst (more than 1.5 g L^{-1}), a saturation level is reached due to the full absorption of the incident light and/or light scattering by the colloidal particles, so that the generation rate of hydrogen becomes slightly lower. In the following, we compared the hydrogen generation activity of the CZS-5 NCAs in the presence of Na_2S/Na_2SO_3 pairs, methanol, and ethanol in neutral and alkaline (5 M NaOH) solutions as electron donors. All these photocatalytic reactions were conducted under visible-light irradiation ($\lambda \geq 420$ nm) using a fixed mass of the catalyst (1 g L^{-1}). The results showed that, for the present system, the S^{2-}/SO_3^{2-} pairs are the most efficient sacrificial electron donors, resulting in a significant reaction enhancement (Fig. S3†).

Furthermore, the photocatalytic hydrogen evolution efficiency was considerably improved after sulfidation of the CZS-5 catalyst. Catalytic results in Fig. 5a show that CZS′-5 outperforms all other samples, showing a hydrogen evolution rate of 30.0 μmol h^{-1} (~1 mmol h^{-1} g_{cat}^{-1}) within 4 h, which is about 1.7 times higher than that of the untreated catalyst. The apparent quantum yield (AQY) for this reaction, assuming that all incident photons are absorbed by the catalyst suspension, is estimated to be 17.6% at 410 ± 10 nm. Combined with further electro- and photochemical studies (see below), we attribute the superior hydrogen evolution efficiency of CZS′-5 to the chemical passivation of defect states (mainly sulfur vacancies arising from the charge compensation of Cu^+ substitution with Zn^{2+} sites). In particular, the light excitation of CZS′-5 generates more surface-reaching electrons for hydrogen evolution, instead of losing a portion to electron–hole recombination at the structure or surface defects. The AQY of the CZS′-5 NCAs is also higher than or comparable to those of other noble-metal-free ZnS-based photocatalysts, such as CdS/ZnS core–shell microparticles (9.3% AQY at 420 nm),[29] $Cd_{0.8}Zn_{0.2}S$ solid-solution particles (10.23% AQY at 420 nm),[30] CdS QD-sensitized $Zn_{1-x}Cd_xS$ solid solution (Cd/Zn ratio = 5) (6.3% at 420 nm),[31] $(Zn_{0.95}Cu_{0.05})_{0.67}Cd_{0.33}S$ solid solution NCs (15.7% AQY at 420 nm),[32] CuS(5.9%)/$Zn_{0.65}Cd_{0.35}S$ nanospheres (8.1% AQY at 420 nm),[33] $AgIn_5S_8$/ZnS heterostructures (3.7% AQY at 420 nm),[34] $Cd_{0.1}Cu_{0.01}Zn_{0.89}S$ particles (9.6% AQY at 420 nm),[35] $Cu(OH)_2$-loaded ZnO/ZnS nanobranches (11.5% AQY at 420 nm),[36] CuS/ZnS porous nanosheets (20% AQY at 420 nm),[37] $(CuAgZnSnS_4)_{0.9}(ZnS)_{0.4}$ mixed crystals (0.25% AQY at 400 nm),[38] Bi (0.3%)-doped ZnS hollow spheres (0.99% AQY at 420 nm)[39] and Ga(0.1%), Cu(0.01%)-co-doped ZnS nanospheres (0.14% AQY at 425 nm).[40] Interestingly, when sulfidation was performed on the starting ZnS NCs or mesoporous network of the cross-linked ZnS NCs to form the sulfurated products (denoted as C/ZS-S′-5 and C/ZS′-5 NCAs, respectively, details in the Experimental section), the resulting catalytic activity was significantly lower; namely, C/ZS-S′-5 and C/ZS′-5 catalysts gave a H_2 production rate of 3.9 and 22.5 μmol h^{-1} over a 3 h reaction period, respectively (Fig. S4†). This further confirms that the photochemical enhancement achieved by the CZS′-5 catalyst for hydrogen evolution is due to the passivation of defect sites generated mainly at the Cu_2S/ZnS interface (as a result of the incorporation of Cu^+ into the ZnS mesostructure).

Results of the repeated photocatalytic hydrogen evolution tests showed that CZS′-5 remains stable during the photocatalytic process. The stability of the catalyst was tested by performing three consecutive 5 h photocatalytic cycles. After each reuse, the catalyst was isolated from the reaction mixture by centrifugation, washed with a polysulfide solution to remove the adsorbed sulfur species, and re-dispersed in a fresh reaction solution. Before each photocatalytic reaction, the reaction cell was de-aerated by purging with argon to remove dissolved oxygen. As shown in Fig. 5b, the CZS′-5 catalyst maintains its photocatalytic activity (within 5% experimental error) and an amount of ~0.39 mmol of H_2 was detected (ca. 8.8 mL STP) after 15 h of irradiation. The small decline of the H_2 evolution rate after three 5 h cycles of reuse may be caused by the mass loss of the catalyst during the recovery process, although minor photocorrosion of the sulfide catalyst during irradiation is a possible explanation. Elemental analysis of the reused catalyst by EDS showed a distribution of Zn and Cu elements with a ~49.1 : 2.6 Zn/Cu molar ratio that corresponds to a Cu content of about 5 mol%, in agreement with the composition of the fresh material (Table S1†). From N_2 physisorption data, the BET surface area of this sample is found to be 102 m^2 g^{-1} and the pore size to be 4.6 nm (Fig. S5a†) which are very close to those of fresh CZS′-5. Also, the TEM study showed that the reused catalyst maintains its crystallinity and structural integrity during catalysis (Fig. S5b and S5c†). In addition, powder XRD and XPS data confirm that the zinc blende structure of ZnS and the chalcocite structure of Cu_2S are well retained after cycle reactions (Fig. S6†), further evidencing the structural stability of the catalyst under the examined conditions.

2.3 Electrochemical properties

The electronic band alignment and photochemical behavior of the CZS mesoporous solids were examined through film formation of the samples on FTO substrates using electrochemical impedance spectroscopy (EIS). Fig. 6a shows the $1/C^2$ versus applied voltage (E) curves and the corresponding linear fits for the mesoporous ZS and CZS NCAs materials, from which the position of the flat-band potentials (E_{FB}) can be determined by extrapolating to $1/C^2 = 0$. This points to an esti-
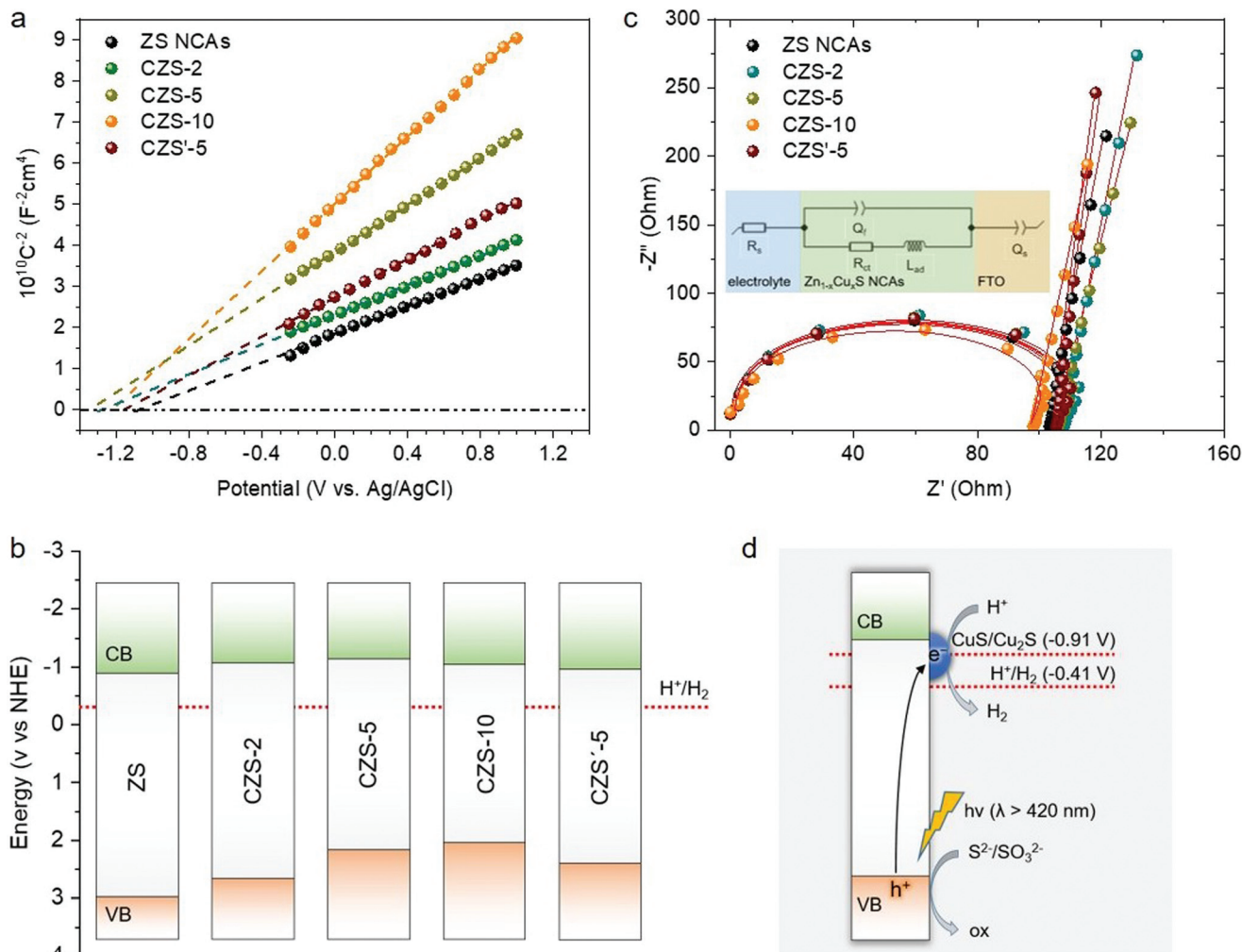
Fig. 6 (a) Mott–Schottky plots where the E_{FB} values were obtained from the intercepts of the extrapolated linear fits of the $1/C^2$ vs. E curves, (b) energy band diagrams and (c) EIS Nyquist spectra and equivalent circuit model (inset) of mesoporous ZS, CZS and CZS'-5 NCAs at an open circuit voltage in a 0.5 M Na$_2$SO$_4$ electrolyte. (d) Schematic illustration for visible light induced interfacial electron transfer from the VB of ZnS to the CuS/Cu$_2$S clusters in the CZS'-5 catalyst (VB: valence band; CB: conduction band). The reduction potentials of the H$^+$/H$_2$ and CuS/Cu$_2$S couples are also given. All the potentials are referred to the normal hydrogen electrode (NHE) at pH 7.

mated E_{FB} value of −0.88 V for ZS and from −1.02 to −1.12 V for the CZS catalysts, see Table 2. The E_{FB} values of the measured samples are expressed in reference to the electrochemical potential of the normal hydrogen electrode (NHE) at pH = 7. Results from the Mott–Schottky plots clearly indicated that the E_{FB} level undergoes a cathodic shift upon Cu$^+$ doping.

Table 2 Electrochemical data (pH 7) for mesoporous ZS, CZS and CZS'-5 NCAs

Sample	Flat band potential, E_{FB} (V vs. NHE)	VB energy, E_v (V vs. NHE)	Donor density, N_d (cm^{-3})
ZS	−0.88	3.00	9.32×10^{16}
CZS-2	−1.07	2.68	8.80×10^{16}
CZS-5	−1.12	2.20	5.56×10^{16}
CZS-10	−1.02	2.07	3.86×10^{16}
CZS'-5	−0.95	2.41	6.74×10^{16}

In addition, the charge donor density (N_d) of CZS progressively decreases from 9.32×10^{16} to 3.86×10^{16} cm^{-3} with increasing Cu doping level, as reflected by the increased slope of the $1/C^2$ vs. E curves (Table 2). Meanwhile, the positive slope of the $1/C^2$ − E lines suggests n-type doping in our samples, that is, the electrons are the majority carriers.

On the basis of the E_{FB} values and optical band gaps, in Fig. 6b we propose the band energy diagram for each catalyst. Here we assumed that the flat band lies very close to the CB edge position for heavily doped n-type ZnS. The VB energy (E_v) is thus calculated to be 2.07 to 3.00 V vs. NHE by subtracting the corresponding band gap values (based on the optical absorption spectra) from the measured E_{FB} energies, as shown in Table 2. It is likely that the negative shift in the E_{FB} potential upon Cu$^+$ doping is due to the formation of mid-gap Cu 3d and sulfur vacancy states near the CB edge of ZnS (n-type dopants), which results in an upshift of the Fermi level.[41] As

This journal is © the Partner Organisations 2020

Inorg. Chem. Front., 2020, 7, 4687–4700 | 4693

for the decrease of N_d concentration in ZnS with increasing Cu$^+$ doping level, it can be explained by the formation of the p–n junction created between ZnS and the Cu$_2$S nanoparticles; Cu$_2$S is a well-known semiconductor with p-type conductivity.[42] In particular, given that the Fermi level of p-type Cu$_2$S (*ca.* 5.1 eV)[43] is positioned well below the Fermi level of n-type ZnS (*ca.* 4.6–4.8 eV),[44] a built-in electrical potential should be established at the Cu$_2$S/ZnS interface. This thus leads to an electron flow from the ZnS CB to Cu$_2$S until the chemical potentials of two semiconductors reach equilibrium. The transfer of photoinduced electrons may lead to a deformation of the band structure, that is, a depletion layer in ZnS and an accumulation layer on the Cu$_2$S surface at the p–n Cu$_2$S/ZnS junction. The formation of a depletion region in the ZnS phase coincides with the observed decrease in the N_d concentration with increasing Cu content in the CZS NCAs.

On the other hand, sulfidation of the CZS-5 NCAs causes a positive shift in E_{FB} level (−0.95 V *vs.* NHE) and an increase in the N_d concentration (6.74×10^{16} cm^{-3}). Since surface (particularly low-coordinated face and edge atoms) termination with S^{2-} ions should not affect the intrinsic doping properties of the CZS-5 material, it is likely that the observed down-shift in the flat-band position is due to the surface-state passivation of the composite structure by S^{2-} ions that suppress the Fermi-level pinning. In particular, the charged surface-states (*i.e.*, mid-gap localized electronic states on the semiconductor surface) can induce a large potential drop across the Helmholtz double layer (V_H), which, however, can be reduced to a large extent by surface passivation.[45] In this case, the Fermi level of the semiconductor becomes almost independent from the allowed energy levels of the bulk and is essentially "pinned" at the energy level of the surface-states. Thus, the Fermi level position and band bending at the surface of the semiconductor will be affected by changes in V_H, as shown in eqn (3).

$$E_{FB} = V_H + \phi_{SC} - 4.5 \qquad (3)$$

where, ϕ_{SC} is the work function of the semiconductor and −4.5 eV is the H$^+$/H$_2$ redox level relative to vacuum.

For a specific solution pH, the Helmholtz layer potential drop depends on the point of zero charge of the semiconductor surface (pH$_{PZC}$) according to eqn (4).

$$V_H = 0.059 \times (pH_{PZC} - pH) \qquad (4)$$

where, pH$_{PZC}$ in an aqueous electrolyte corresponds to the pH value where $V_H = 0$.

To elucidate this possibility, the effect of surface sulfide ions on the charge of CZS colloids was probed through zeta potential measurements using a 0.5 M Na$_2$SO$_4$ solution at pH 7 (similarly to the EIS experiments). The zeta potentials of the CZS-5 and CZS′-5 NCAs were measured as −12.7 and −10.2 mV, respectively. Clearly, the particles in these suspensions are all negatively charged and their corresponding pH$_{PZC}$ values are lower than 7, consistent with literature results (ZnS has a pH$_{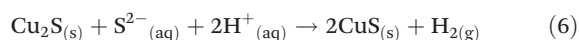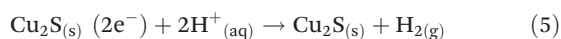PZC}$ value of 4.2).[46] Moreover, the less negative zeta potential of the sulfurated sample (CZS′-5) implies a more positive V_H value at the ZnS/Cu$_2$S/solution junction, which, according to eqn (3), is in line with the observed positive (anodic) shift of E_{FB} (see Table 2). As for the slight increase in the carrier density (N_d) of CZS′-5, this could be tentatively attributed to the lower recombination rate and faster electron transport at the Cu$_2$S/ZnS interface. This assumption is also supported by further electrochemical and photoluminescence studies.

EIS Nyquist measurements of the synthesized electrodes (FTO substrates covered with ZS and the CZS NCAs samples) allowed us to derive information on the charge transfer properties of the assembled nanostructures (Fig. 6c). The charge-transport resistance (R_{ct}) of drop-cast films can be determined from fitting the EIS data using an equivalent circuit model (the inset of Fig. 6c) and the values were obtained as 100.5 Ω for ZS and as 102.6, 102.9 and 105.4 Ω for CZS-2, CZS-5 and CZS-10, respectively. The descending trend of the charge transfer efficiency with increasing Cu content indicates explicitly that Cu$^+$ doping contributes to a lower electron mobility in the mesoporous structures. In particular, the high level of R_{ct} suggests a diminished charge transfer presumably along the composite structure, which correlates with the loss of surface-reaching electrons to interface recombination at the Cu$_2$S/ZnS junction. In contrast, the sulfurated CZS′-5 catalyst exhibited the lowest R_{ct} resistance (95.6 Ω) among the examined samples, which can be attributed to the smooth charge transfer within the composite Zn–S–Cu structure due to relatively low defect concentrations at the Cu$_2$S/ZnS interface. Note that the EIS slope of the linear portion for CZS′-5 is comparable with that of CZS-5 in the low frequency region (Fig. 6c), indicating that the diffusion resistance (R_s) is similar in these materials. This implies that the diffusion rate of the electrolyte to the surface-active sites does not specify the effectiveness of the catalysts, and other inherent properties, such as electrical conductivity and charge mobility, may have a more profound influence on the underlying photocatalytic hydrogen evolution behavior. In agreement with this, further photocurrent measurements performed at an applied voltage of 1 V (see details in the Experimental section) showed that the sulfurated CZS′-5 catalyst generates a higher photocurrent density (13.5 mA cm^{-2}) than does CZS-5 (10.3 mA cm^{-2}) under 400–800 nm light irradiation. This means that the CZS′-5 catalyst effectively reduces the charge recombination within the composite structure and affords a higher photoinduced electron transfer and separation efficiency compared to CZS-5. In combination with the above electrochemical results, these findings provide an interesting strategy for enhancing free exciton dissociation and charge transfer properties at the interface of the sulfide treated Cu$_2$S/ZnS junctions. The charge transfer efficiency of the CZS heterostructures is furthermore evident from photo-luminescence (PL) spectroscopy analysis. Fig. S7† shows the comparison of the PL spectra of mesoporous ZS with those of the CZS-5 and sulfurated CZS′-5 samples at an excitation wavelength of 330 nm. ZS shows a broad PL signal at ~442 nm, which is related to the radiative

4694 | *Inorg. Chem. Front.*, 2020, **7**, 4687–4700

This journal is © the Partner Organisations 2020

relaxation of excitons through shallow in-gap levels.[47] This suggests that defect-localized states such as sulfur vacancies (n-type dopants) are present near the surface of the ZnS NCs, which serve as recombination centers for electrons and holes. In contrast, the CZS-5 heterostructure shows a noticeable decrease of the PL emission, which is attributed to the efficient interfacial electron transfer along the Cu_2S/ZnS junctions. Of note, after treatment with S^{2-}, the corresponding defect-related emission (at 442 nm) of CZS′-5 almost vanished, again confirming that the defect states within the Zn–S–Cu composite structure are efficiently suppressed, leading to a higher delocalization of electron–hole pairs, in line with the above EIS and photocurrent experiments.

The above analyses directly demonstrate that Cu^+ doping in the ZnS NCs prominently affects their optical response and charge transport properties. Overall the Cu_2S/ZnS junctions facilitate the spatial distribution of charge carriers through the appropriate alignment in the band-edge positions of the composites. This effect definitely has a profound impact on the photocatalytic behavior of the CZS heterostructures. The mechanism for photocatalytic H_2 evolution in the CZS NCAs can be depicted as in Fig. 6d. It is considered that, under visible light irradiation, Cu_2S gets excited and generates electron–hole pairs; Cu_2S has an energy band gap of about 1.2–1.8 eV.[48] In addition, during the course of irradiation, a fraction of photoexcited electrons from the VB of ZnS may be transferred to the CuS clusters (formed by the partial oxidation of Cu^+ from S^{2-} ions according to eqn (2)), causing their partial reduction to Cu_2S ($E° = -0.91$ V vs. NHE, pH = 7). Given that the transition energy from the VB of ZnS to Cu_2S/CuS is approximately 2.9–3.0 eV (~415–430 nm), this electron transfer appears feasible. Note that the absence of the XPS signal corresponding to Cu^{2+} in the CZS′-5 catalyst examined after catalysis is highly related to this reaction scheme (Fig. S6d†). In this respect, the Cu_2S/CuS species can also function as cocatalysts facilitating the charge separation through the interfacial electron transfer from ZnS to Cu_2S/CuS. Besides, photoexcited Cu_2S may also react with protons and sulfide ions from the solution to form molecular hydrogen, and even CuS, according to the following equations:

$$Cu_2S_{(s)} \; (2e^-) + 2H^+_{(aq)} \rightarrow Cu_2S_{(s)} + H_{2(g)} \tag{5}$$

$$Cu_2S_{(s)} + S^{2-}_{(aq)} + 2H^+_{(aq)} \rightarrow 2CuS_{(s)} + H_{2(g)} \tag{6}$$

Meanwhile, driven by the internal electron field at the p–n junction interface, the photogenerated holes in the VB of ZnS can migrate to the VB of the Cu_2S NCs where they effectively oxidize the sacrificial reagents (S^{2-}/SO_3^{2-}). Therefore, an efficient charge separation and transfer is successfully achieved through the p–n junctions of the Cu_2S and ZnS NCs, leading to an enhanced photocatalytic hydrogen production activity.

3. Conclusions

In summary, we have successfully prepared high-surface-area mesoporous networks of Cu-doped ZnS NCs (CZS-n NCAs, n = 2, 5, 10) as efficient catalysts for the hydrogen evolution reaction. The CZS catalysts are composed of tightly-connected cubic zinc blende ZnS and cubic chalcocite Cu_2S nanocrystals and show a porous structure between the nanocrystal networks with a large surface area (ca. 142–314 m^2 g^{-1}) and narrow pore size distribution (ca. 4.4–4.8 nm), according to X-ray diffraction, X-ray photoelectron spectroscopy, high-resolution TEM and electron diffraction. Using a combination of spectroscopic and photo- and electrochemical characterization techniques, we demonstrate that Cu^+ doping has a prominent impact on the photocatalytic performance by extending the visible-light response and improving the charge separation properties of the CZS nano-heterostructures. In this work, surface defect engineering of the CZS assemblies with sulfide ions can be considered an effective way to decrease the quantity of intrinsic defects (sulfur vacancies) which are detrimental to exciton separation and, thus, photocatalytic reactions. The effectiveness of this approach is proved by the efficient charge transfer at the Cu_2S/ZnS interface and higher photocatalytic hydrogen evolution activity of the sulfurated CZS′-5 catalyst. We obtained a hydrogen evolution rate of 30.0 μmol h^{-1} under visible light, and determined an AQY of 17.6% at wavelength λ = 410 nm. The activity of this catalyst is superior to those of previously reported ZnS-based materials. This approach can be considered an interesting strategy for enhancing the interface charge transfer properties and hydrogen evolution performance of metal sulfides by surface defect engineering with sulfide ions.

4. Experimental

4.1 Synthesis of 5 nm ZnS NCs

In a typical synthesis, 20 mmol of 3-mercaptopropionic acid (MPA) was added into a 50 mL aqueous solution containing 10 mmol of $ZnCl_2$, and the solution pH was adjusted to 10 using ammonium hydroxide (NH_4OH). Then, 10 mmol of $Na_2S \cdot 9H_2O$ dissolved in 50 mL of DI water was slowly added to the above solution and the reaction mixture was stirred at ambient temperature for 1 h. The MPA-capped ZnS NCs were isolated by precipitation, with the addition of 2-propanol followed by centrifugation, and the obtained NCs were finally dried at 60 °C for 24 h.

4.2 Preparation of mesoporous ZnS NCAs

Porous networks of ZnS NCs (denoted as ZS NCAs) were prepared according to our previously reported method.[19] Briefly, 250 mg of block copolymer Brij-58 ($HO(CH_2CH_2O)_{20}C_{16}H_{33}$, M_n ~ 1124) was dissolved in 2.5 mL of water in a 50 ml glass beaker. To this solution, a colloidal solution of MPA-capped ZnS NCs (1.7 mmol in 2.5 mL water) was added and the resultant dispersion was stirred for 1 h. Afterwards, 2 mL of H_2O_2

This journal is © the Partner Organisations 2020

Inorg. Chem. Front., 2020, **7**, 4687–4700 | **4695**

(1 wt%) solution was slowly added and the mixture was kept under stirring until gelation was observed (typically within ~1 h). The obtained mixture was then placed in an oven for 3 days at 40 °C to evaporate the solvent under static conditions. Finally, the polymer template was removed by soaking the gel product once in 20 mL of ethanol for 2 h and three times in 20 mL of water for 15 min. The mesoporous solids were filtered under vacuum, washed several times with water and ethanol, and dried at 60 °C for 12 h.

4.3 Preparation of mesoporous Cu-doped ZnS NCAs

Porous networks of Cu-doped ZnS NCs were synthesized *via* a partial cation exchange reaction of Zn^{2+} with Cu^+ ions. In particular, 100 mg of the as-prepared ZnS mesoporous material (ZS NCAs) was dispersed in 20 mL of water containing different amounts of CuCl. A series of Cu-doped ZnS NC assemblies with 2, 5 and 10 mol% of Cu content (denoted as CZS-*n* NCAs; *n* = 2, 5 and 10) were obtained by varying the initial Cu^+ concentration in the reaction mixture.

For a comparative study, Cu-doped ZnS NC assemblies with 5 mol% Cu^{2+} content (denoted as C(II)ZS-5 NCAs) were also prepared following a similar procedure, using $CuCl_2$ as a precursor.

4.4 Sulfidation of mesoporous Cu/ZnS frameworks

A mesoporous network of sulfide-treated 5% Cu-doped ZnS NCs (denoted as CZS′-5 NCAs) was prepared as follows: 0.25 mmol of the CZS-5 catalyst and 0.25 mmol of Na_2S were added into 10 mL of water, and the resulting mixture was kept under constant stirring for 2 h. The sulfurated sample was isolated by centrifugation, washed several times with water and ethanol, and dried at 60 °C for 12 h.

Other sulfurated Cu-doped ZnS samples were also prepared as following: 1 mmol of colloidal ZnS NCs and 1 mmol of Na_2S were dispersed in 10 mL of water, and the mixture was kept under stirring for 2 h at room temperature. Afterwards, the S^{2-}-treated NCs were isolated by precipitation with the addition of 2-propanol, and dried at 60 °C for 24 hours. Next, a mesoporous network of 5% Cu-doped ZnS NCs (denoted as C/ZS-S′-5) was prepared following the method as described above, by using S^{2-}-treated ZnS NCs as starting building blocks. In a different experiment, 1 mmol of mesoporous ZS NCAs was dispersed in 10 mL of water containing 1 mmol of Na_2S and the resulting mixture was stirred for 2 h. The product was isolated by centrifugation, washed several times with water and ethanol, and dried at 60 °C for 12 h. As a next step, the S^{2-}-treated ZnS mesoporous sample was doped with Cu^+ (5 mol%) following the method as described above, giving the sulfide-treated 5% Cu/ZnS mesoporous sample (denoted as C/ZS′-5).

4.5 Physical characterization

Powder X-ray diffraction (XRD) patterns were collected using a PANalytical X'Pert Pro X-ray diffractometer operated at 45 kV and 40 mA using Cu Kα radiation (λ = 1.5418 A). Elemental microprobe analysis was performed using a JEOL JSM-6390LV scanning electron microscope (SEM) equipped with an INCA PentaFETx3 energy-dispersive X-ray spectroscopy (EDS) detector (Oxford Instruments, UK). EDS analysis was performed at least four times for each sample at an accelerating voltage of 20 kV and 60 s accumulation time. Transmission electron microscopy (TEM) images were obtained using a JEOL JEM-2100 electron microscope operated at 200 kV. Samples were prepared by drying an ethanolic dispersion of particles on a holey carbon-coated Cu grid. Nitrogen adsorption–desorption isotherms were obtained at −196 °C using a Quantachrome NOVA 3200e analyzer. Before analysis, all the samples were outgassed at 80 °C for 12 h under vacuum (<10^{-5} Torr). The specific surface areas were calculated by applying the Brunauer–Emmett–Teller (BET) method[49] to the adsorption data and the pore volumes were calculated from the amount of adsorbed N_2 at a relative pressure (P/P_0) of 0.98. The pore size distributions were derived from the adsorption isotherms using the non-local density functional theory (NLDFT) method.[50] X-ray photoelectron spectroscopy (XPS) measurements were carried out using a non-monochromatic Al K_α line at 1486.6 eV (12 kV with 20 mA anode current) and a Leybold LH EA11 electron energy analyzer operated at a constant pass energy of 100 eV and pressure of 2×10^{-8} mbar. The catalyst powder was pressed on a thin Pb sheet and the analyzed area was a 1.5×5 mm^2 rectangle, placed near the center of the powder-covered area on each specimen surface. In all XPS spectra, the binding energy of the predominant aliphatic contribution to the C 1s peak at 284.8 eV was used as a charge reference. UV–vis diffuse reflectance spectra were recorded on a PerkinElmer Lambda 950 optical spectrophotometer. $BaSO_4$ powder was used as a standard (100% reflectance). The absorption spectra were converted from diffuse reflectance data using the Kubelka–Munk function: $\alpha/S = (1 − R)^2/(2R)$, where R is the measured reflectance and α and S are the absorption and scattering coefficients, respectively.[51] The energy bandgap (E_g) of semiconductors was calculated from the Tauc plots, that is, $(ah\nu)^2$ as a function of energy ($h\nu$) plots.[52] The zeta potential of the materials was measured using a Malvern Zetasizer Nano ZS90 zeta potential analyzer after dispersing the samples in a 0.5 M Na_2SO_4 aqueous solution. The pH of the solution was adjusted to 7 with 0.1 M NaOH or 0.1 M H_2SO_4. Photoluminescence (PL) spectra were recorded on a Lumina Fluorescence spectrometer (Thermo Fisher Scientific) equipped with a 150 W xenon lamp.

4.6 Electrochemical measurements

Electrochemical impedance spectroscopy (EIS) and Mott–Schottky measurements were performed in a 0.5 M Na_2SO_4 aqueous electrolyte (pH = 7) using a Metrohm Autolab PGSTAT 302N potentiostat. A three-electrode electrochemical cell with a Pt wire as the counter electrode and Ag/AgCl (3 M KCl) as the reference electrode was used to study the samples. Mott–Schottky plots were obtained at 1 kHz, using a 10 mV alternating current (AC) voltage amplitude. The measured flat-band potentials were converted to the normal hydrogen electrode (NHE) scale using the Nernst equation $E_{NHE} = E_{Ag/AgCl} + 0.21 +$

4696 | *Inorg. Chem. Front.*, 2020, **7**, 4687–4700

This journal is © the Partner Organisations 2020

$0.059 \times$ pH. For Nyquist plots, a different current output was measured throughout a frequency range from 1 Hz to 1 MHz using a small AC perturbation of 20 mV, under open-circuit potential conditions. All the EIS experiments were conducted in the dark.

The working electrodes were fabricated as follows: 10 mg of each sample was ultrasonically mixed with 1 mL of deionized water to form a homogeneous suspension. Glass slides (1.5 × 2 cm^2) coated with a fluorine-doped tin oxide (FTO, 9 Ω sq^{-1}) substrate were cleaned thoroughly by sonication in acetone and then in isopropanol for 15 min and dried at 100 °C for 10 min. Next, the FTO substrates were further treated with a UV-ozone plasma for 5 min. The samples were drop-cast into the FTO substrates, which were masked with an epoxy resin to leave an exposure area of 1.0 cm^2, and heated for 30 min at 60 °C.

4.7 Photoelectrochemical measurements

Photoelectrochemical measurements were carried out in an air-tight three-electrode cell with the samples as the working electrode (1 cm^2 illumination area), Ag/AgCl (3 M KCl) as the reference electrode, and a Pt wire as the counter electrode. Photocurrent data were collected with a 5 M KOH aqueous electrolyte at a potential of 1 V (*vs.* Ag/AgCl). Before analysis, the electrolyte was purged with N$_2$ for 30 min to remove the oxygen. Photocurrent densities of the samples were measured using a Metrohm Autolab PGSTAT 302N potentiostat coupled with a neutral white light-emitting diode (WLED, λ = 400–800 nm).

4.8 Photocatalytic hydrogen evolution study

Photocatalytic experiments for hydrogen evolution were performed in an airtight Pyrex glass reactor. In a typical experiment, 20 mg of the catalyst was dispersed with stirring in 20 mL of an aqueous solution containing 0.35 M Na$_2$S and 0.25 M Na$_2$SO$_3$, and then the mixture was deaerated with Ar gas for at least 30 min. The reaction solution was cooled to 20 ± 2 °C using a water-cooling system and irradiated at $\lambda \geq$ 420 nm light using a 300 W Xenon lamp (Variac Cermax). The generated H$_2$ was detected by taking 100 μL of gas from the headspace of the reactor using a gastight syringe and analyzed by using a Shimadzu GC-2014 gas chromatograph equipped with a thermal conductivity detector (TCD), using Ar as the carrier gas.

The apparent quantum yield, AQY = $(2 \times N_{H_2})/N_{hv}$ where N_{H_2} and N_{hv} are the numbers of evolved H$_2$ molecules and incident photons, respectively, was estimated by obtaining the amount of evolved hydrogen at a λ = 410 ± 10 nm irradiation wavelength. The incident photon number was determined with a StarLite power meter equipped with an FL400A-BB-50 thermal sensor (Ophir Optronics Ltd).

Conflicts of interest

There are no conflicts to declare.

Acknowledgements

Notes and references

1 D. A. Hickman and L. D. Schmidt, Production of Syngas by Direct Catalytic Oxidation of Methane, *Science*, 1993, **259**, 343; J. R. Rostrup-Nielsen, New Aspects of Syngas Production and Use, *Catal. Today*, 2000, **63**, 159.

2 B. A. Pinaud, J. D. Benck, L. C. Seitz, A. J. Forman, Z. Chen, T. G. Deutsch, B. D. James, K. N. Baum, G. N. Baum, S. Ardo, H. Wang, E. Miller and T. F. Jaramillo, Technical and Economic Feasibility of Centralized Facilities for Solar Hydrogen Production via Photocatalysis and Photoelectrochemistry, *Energy Environ. Sci.*, 2013, **6**, 1983.

3 J. H. Montoya, L. C. Seitz, P. Chakthranont, A. Vojvodic, T. F. Jaramillo and J. K. Nørskov, Materials for Solar Fuels and Chemicals, *Nat. Mater.*, 2017, **16**, 70; T. Hisatomi, J. Kubota and K. Domen, Recent Advances in Semiconductors for Photocatalytic and Photoelectrochemical Water Splitting, *Chem. Soc. Rev.*, 2014, **43**, 7520; M. R. Gholipour, C.-T. Dinh, F. Béland and T.-O. Do, Nanocomposite Heterojunctions as Sunlight-Driven Photocatalysts for Hydrogen Production from Water Splitting, *Nanoscale*, 2015, **7**, 8187; L. Nie and Q. Zhang, Recent Progress in Crystalline Metal Chalcogenides as Efficient Photocatalysts for Organic Pollutant Degradation, *Inorg. Chem. Front.*, 2017, **4**, 1953; Y. Liu, P. D. Kanhere, C. L. Wong, Y. Tian, Y. Feng, F. Boey, T. Wu, H. Chen, T. J. White, Z. Chen and Q. Zhang, Hydrazine-hydrothermal Method to Synthesize Three-dimensional Chalcogenide Framework for Photocatalytic Hydrogen Generation, *J. Solid State Chem.*, 2010, **183**, 2644.

4 X. Li, J. Yu, J. Low, Y. Fang, J. Xiao and X. Chen, Engineering Heterogeneous Semiconductors for Solar Water Splitting, *J. Mater. Chem. A*, 2015, **3**, 2485.

5 J. Zhou, H. L. Zhuang and H. Wang, Layered Tetragonal Zinc Chalcogenides for Energy-Related Applications: from Photocatalysts for Water Splitting to Cathode Materials for Li-ion Batteries, *Nanoscale*, 2017, **9**, 17303; Q. H. Nguyen, T. Park and J. Hur, Enhanced Cycle Stability of Zinc Sulfide Anode for High-Performance Lithium-Ion Storage: Effect of Conductive Hybrid Matrix on Active ZnS, *Nanomaterials*, 2019, **9**, 1221; G. Tian, Z. Zhao, A. Sarapulova, C. Das, L. Zhu, S. Liu, A. Missiul, E. Welter, J. Maibach and S. Dsoke, Understanding the Li-ion Storage Mechanism in a Carbon Composited Zinc Sulfide Electrode, *J. Mater. Chem. A*, 2019, **7**, 15640; Y. Feng, Y. Zhang, Y. Wei, X. Song, Y. Fu and V. S. Battaglia, A ZnS Nanocrystal/Reduced

This journal is © the Partner Organisations 2020

Inorg. Chem. Front., 2020, **7**, 4687–4700 | **4697**

Graphene Oxide Composite Anode with Enhanced Electrochemical Performances for Lithium-ion Batteries, *Phys. Chem. Chem. Phys.*, 2016, **18**, 30630.

6 M. Kamruzzaman, The Effect of ZnO/ZnSe Core/Shell Nanorod Arrays Photoelectrodes on PbS Quantum Dot Sensitized Solar Cell Performance, *Nanoscale Adv.*, 2020, **2**, 286; Z. A. Fard and H. Dehghani, Investigation of the Effect of Sr-doped in ZnSe Layers to Improve Photovoltaic Characteristics of ZnSe/CdS/CdSe/ZnSe Quantum Dot Sensitized Solar Cells, *Sol. Energy*, 2019, **184**, 378; D. Li, S. Hao, G. Xing, Y. Li, X. Li, L. Fan and S. Yang, Solution Grown Single-Unit-Cell Quantum Wires Affording Self-Powered Solar-Blind UV Photodetectors with Ultrahigh Selectivity and Sensitivity, *J. Am. Chem. Soc.*, 2019, **141**(8), 3480; X. Li, J. Yang, Q. Jiang, H. Lai, S. Li, J. Xin, W. Chu and J. Hou, Low-Temperature Solution-Processed ZnSe Electron Transport Layer for Efficient Planar Perovskite Solar Cells with Negligible Hysteresis and Improved Photostability, *ACS Nano*, 2018, **12**(6), 5605.

7 A. Serrà, R. Artal, J. García-Amorós, B. Sepúlveda, E. Gómez, J. Nogués and L. Philippe, Hybrid Ni@ZnO@ZnS–Microalgae for Circular Economy: A Smart Route to the Efficient Integration of Solar Photocatalytic Water Decontamination and Bioethanol Production, *Adv. Sci.*, 2020, **7**, 1902447; P. Li and T. He, Common-cation Based Z-scheme ZnS@ZnO Core-Shell Nanostructure for Efficient Solar-Fuel Production, *Appl. Catal., B*, 2018, **238**, 518; S. Yu, X.-B. Fan, X. Wang, J. Li, Q. Zhang, A. Xia, S. Wei, L.-Z. Wu, Y. Zhou and G. R. Patzke, Efficient Photocatalytic Hydrogen Evolution with Ligand Engineered All-Inorganic InP and InP/ZnS Colloidal Quantum Dots, *Nat. Commun.*, 2018, **9**, 4009; J. Lee, S. Ham, D. Choi and D.-J. Jang, Facile Fabrication of Porous ZnS Nanostructures with a Controlled Amount of S Vacancies for Enhanced Photocatalytic Performances, *Nanoscale*, 2018, **10**, 14254; X. Hao, J. Zhou, Z. Cui, Y. Wang, Y. Wang and Z. Zou, Zn-Vacancy Mediated Electron-Hole Separation in ZnS/g-C₃N₄ Heterojunction for Efficient Visible-Light Photocatalytic Hydrogen Production, *Appl. Catal., B*, 2018, **229**, 41.

8 J. S. Hu, L. L. Ren, Y. G. Guo, H. P. Liang, A. M. Cao, L. J. Wan and C. L. Bai, Mass Production and High Photocatalytic Activity of ZnS Nanoporous Nanoparticles, *Angew. Chem., Int. Ed.*, 2005, **44**, 1269.

9 G. Wang, B. Huang, Z. Li, Z. Lou, Z. Wang, Y. Dai and M.-H. Whangbo, Synthesis and Characterization of ZnS with Controlled Amount of S Vacancies for Photocatalytic H₂ Production under Visible Light, *Sci. Rep.*, 2015, **5**, 8544.

10 S. Khan, H. Choi, D. Kim, S. Y. Lee, Q. Zhu, J. Zhang, S. Kim and S.-H. Cho, Self-Assembled Heterojunction of Metal Sulfides for Improved Photocatalysis, *Chem. Eng. J.*, 2020, **395**, 125092.

11 J. Zhang, Q. Xu, S. Z. Qia and J. Yu, Enhanced Visible-Light H₂ Production Activity of Copper Modified Zn$_x$Cd$_{1-x}$S, *ChemSusChem*, 2013, **6**, 2009; I. Tsiji, H. Kato, H. Kobayashi and A. Kudo, Photocatalytic H2 Evolution

Reaction from Aqueous Solutions over Band Structure-Controlled (AgIn)$_x$, Zn$_{2(1-x)}$S₂ Solid Solution Photocatalysts with Visible-Light Response and their Surface Nanostructures, *J. Am. Chem. Soc.*, 2004, **126**, 13406.

12 J. Zhang, Y. Wang, J. Zhang, Z. Lin, F. Huang and J. Yu, Enhanced Photocatalytic Hydrogen Production Activities of Au-Loaded ZnS Flowers, *ACS Appl. Mater. Interfaces*, 2013, **5**, 1031; A. Iwase, K. Li and A. Kudo, Decomposition of an Aqueous Ammonia Solution as a Photon Energy Conversion Reaction using a Ru-Loaded ZnS Photocatalyst, *Chem. Commun.*, 2018, **54**, 6117.

13 Y.-C. Zhu, Y. Bando and L.-W. Yin, Design and Fabrication of BN-Sheathed ZnS Nanoarchitectures, *Adv. Mater.*, 2004, **16**, 331.

14 S. Xiao, W. Dai, X. Liu, D. Pan, H. Zou, G. Li, G. Zhang, C. Su, D. Zhang, W. Chen and H. Li, Microwave–Induced Metal Dissolution Synthesis of Core–Shell Copper Nanowires/ZnS for Visible Light Photocatalytic H₂ Evolution, *Adv. Energy Mater.*, 2019, **9**, 1900775.

15 T. Arai, S. Senda, Y. Sato, H. Takahashi, K. Shinoda, B. Jeyadevan and K. Tohji, Cu-doped ZnS Hollow Particle with High Activity for Hydrogen Generation from Alkaline Sulfide Solution under Visible Light, *Chem. Mater.*, 2008, **20**, 1997.

16 Z. Mei, B. Zhang, J. Zheng, S. Yuan, Z. Zhuo, X. Meng, Z. Chen, K. Amine, W. Yang, L. W. Wang, W. Wang, S. Wang, Q. Gong, J. Li, F. S. Liu and F. Pan, Tuning Cu Dopant of Zn$_{0.5}$Cd$_{0.5}$S Nanocrystals Enables High-Performance Photocatalytic H₂ Evolution from Water Splitting under Visible-Light Irradiation, *Nano Energy*, 2016, **26**, 405.

17 I. T. Papadas, I. Vamvasakis, I. Tamiolakis and G. S. Armatas, Templated Self-Assembly of Colloidal Nanocrystals into Three-Dimensional Mesoscopic Structures: A Perspective on Synthesis and Catalytic Prospects, *Chem. Mater.*, 2016, **28**, 2886.

18 L. G. Sillen and A. E. Martell, Stability Constants of Metal-Ion Complexes, in *Lange's Handbook*, The Chemical Society, London, 1964, pp. 8–11.

19 I. Vamvasakis, K. S. Subrahmanyam, M. G. Kanatzidis and G. S. Armatas, Template-Directed Assembly of Metal–Chalcogenide Nanocrystals into Ordered Mesoporous Networks, *ACS Nano*, 2015, **9**, 4419.

20 S. W. Gaarenstroom and N. Winograd, Initial and Final-State Effects in Esca Spectra of Cadmium and Silver-Oxides, *J. Chem. Phys.*, 1977, **67**, 3500; R. Islam and D. R. Rao, X-ray Photoelectron Spectroscopy of Zn$_{1-x}$Cd$_x$Se Thin Films, *J. Electron Spectrosc. Relat. Phenom.*, 1996, **81**, 69; E. Agostinelli, C. Battistoni, D. Fiorani, G. Mattogno and M. Nogues, An XPS Study of the Electronic Structure of the Zn$_x$Cd$_{1-x}$Cr₂X₄ (X=S, Se) Spinel System, *J. Phys. Chem. Solids*, 1989, **50**, 269.

21 L. S. Dake, D. R. Baer and J. M. Zachara, Auger Parameter Measurements of Zinc Compounds Relevant to Zinc Transport in the Environment, *Surf. Interface Anal.*, 1989, **14**, 71.

4698 | *Inorg. Chem. Front.*, 2020, **7**, 4687–4700

This journal is © the Partner Organisations 2020

22 Y. J. Lu and J. H. Jia, The Effect of Complexing Agent on Crystal Growth, Structure and Properties of Nanostructured $Cu_{2-x}S$ Thin Films, *Chin. Chem. Lett.*, 2014, **25**, 1473; I. Nakai, Y. Sugitani, K. Nagashima and Y. Niwa, X-ray Photoelectron Spectroscopic Study of Copper Minerals, *J. Inorg. Nucl. Chem.*, 1978, **40**, 789; M. C. Biesinger, Advanced Analysis of Copper X-ray Photoelectron Spectra, *Surf. Interface Anal.*, 2017, **49**, 1325.

23 P. Liu and E. J. M. Hensen, Highly Efficient and Robust Au/$MgCuCr_2O_4$ Catalyst for Gas-Phase Oxidation of Ethanol to Acetaldehyde, *J. Am. Chem. Soc.*, 2013, **135**, 14032.

24 F. Severino, J. L. Brito, J. Laine, J. L. G. Fierro and A. L. Agudo, Nature of Copper Active Sites in the Carbon Monoxide Oxidation on $CuAl_2O_4$ and $CuCr_2O_4$ Spinel Type Catalysts, *J. Catal.*, 1998, **177**, 82; M. Kundu, T. Hasegawa, K. Terabe, K. Yamamoto and M. Aono, Structural Studies of Copper Sulfide Films: Effect of Ambient Atmosphere, *Sci. Technol. Adv. Mater.*, 2008, **9**, 035011.

25 A. B. F. Martinson, S. C. Riha, E. Thimsen, J. W. Elam and M. J. Pellin, Structural, Optical, and Electronic Stability of Copper Sulfide Thin Films Grown by Atomic Layer Deposition, *Energy Environ. Sci.*, 2013, **6**, 1868.

26 M. Thommes, Physical Adsorption Characterization of Nanoporous Materials, *Chem. Ing. Tech.*, 2010, **82**, 1059.

27 W. He, C. Wang, H. Li, X. Deng, X. Xu and T. Zhai, Ultrathin and Porous $Ni_3S_2/CoNi_2S_4$ 3D-Network Structure for Superhigh Energy Density Asymmetric Supercapacitors, *Adv. Energy Mater.*, 2017, **21**, 1700983.

28 K. Sooklal, B. S. Cullumn, S. M. Angel and C. J. Murphy, Photophysical Properties of ZnS Nanoclusters with Spatially Localized Mn^{2+}, *J. Phys. Chem.*, 1996, **100**, 4551.

29 Y. Lin, Q. Zhang, Y. Li, Y. Liu, K. Xu, J. Huang, X. Zhou and F. Peng, The Evolution from a Typical Type-I CdS/ZnS to Type-II and Z-Scheme Hybrid Structure for Efficient and Stable Hydrogen Production under Visible Light, *ACS Sustainable Chem. Eng.*, 2020, **8**(11), 4537.

30 K. Zhang, D. W. Jing, C. J. Xing and L. J. Guo, Significantly Improved Photocatalytic Hydrogen Production Activity over $Cd_{1-x}Zn_xS$ Photocatalysts Prepared by a Novel Thermal Sulfuration Method, *Int. J. Hydrogen Energy*, 2007, **32**, 4685.

31 J. Yu, J. Zhang and M. Jaroniec, Preparation and Enhanced Visible-Light Photocatalytic H_2-Production Activity of CdS Quantum Dots-Sensitized $Zn_{1-x}Cd_xS$ Solid Solution, *Green Chem.*, 2010, **12**, 1611.

32 W. Zhang, Z. Y. Zhong, Y. S. Wang and R. Xu, Doped Solid Solution: $(Zn_{0.95}Cu_{0.05})_{1-x}Cd_xS$ Nanocrystals with High Activity for H_2 Evolution from Aqueous Solutions under Visible Light, *J. Phys. Chem. C*, 2008, **112**, 17635.

33 W. Zhang and R. Xu, Surface Engineered Active Photocatalysts without Noble Metals: $CuS–Zn_xCd_{1-x}S$ Nanospheres by One-Step Synthesis, *Int. J. Hydrogen Energy*, 2009, **34**, 8495.

34 S. Zhu, Y. Zhang, X. Qian, X. Wang and W. Su, Zn Defect-Mediated Z-Scheme Electron-Hole Separation in $AgIn_5S_8/$ZnS Heterojunction for Enhanced Visible-Light

Photocatalytic Hydrogen Evolution, *Appl. Surf. Sci.*, 2020, **504**, 144396.

35 G. J. Liu, L. Zhao, K. J. Ma and L. J. Guo, Photocatalytic H_2 Evolution under Visible Light Irradiation on a Novel $Cd_xCu_yZn_{1-x-y}S$ Catalyst, *Catal. Commun.*, 2008, **9**, 126.

36 P. Madhusudan, Y. Wang, B. N. Chandashekar, W. Wang, J. Wang, J. Miao, R. Shi, Y. Liang, G. Mi and C. Cheng, Nature Inspired ZnO/ZnS Nanobranch-Like Composites, Decorated with $Cu(OH)_2$ Clusters for Enhanced Visible-Light Photocatalytic Hydrogen Evolution, *Appl. Catal., B*, 2019, **253**, 379.

37 J. Zhang, J. Yu, Y. Zhang, Q. Li and J. R. Gong, Visible Light Photocatalytic H_2-Production Activity of CuS/ZnS Porous Nanosheets Based on Photoinduced Interfacial Charge Transfer, *Nano Lett.*, 2011, **11**, 4774.

38 S. Ikeda, T. Nakamura, T. Harada and M. Matsumura, Multicomponent Sulfides as Narrow Gap Hydrogen Evolution Photocatalysts, *Phys. Chem. Chem. Phys.*, 2010, **42**, 13943.

39 J. Zhang, S. Liu, J. Yu and M. Jaroniec, A Simple Cation Exchange Approach to Bi-doped ZnS Hollow Spheres with Enhanced UV and Visible-Light Photocatalytic H_2-Production Activity, *J. Mater. Chem.*, 2011, **21**, 14655.

40 M. Kimi, L. Yuliati and M. Shamsuddin, Preparation of High Activity Ga and Cu Doped ZnS by Hydrothermal Method for Hydrogen Production under Visible Light Irradiation, *J. Nanomater.*, 2015, **2015**, 195024.

41 J. J. Wu and G. J. Lee, Sonochemical Synthesis of Zinc Sulfide Photocatalysts and Their Environmental Applications, in *Handbook of Ultrasonics and Sonochemistry*, Springer, Singapore, 2016, pp. 867–899.

42 Z. C. Wu, C. Pan, Z. Y. Yao, Q. R. Zhao and Y. Xie, Large-Scale Synthesis of Single-Crystal Double-Fold Snowflake Cu_2S Dendrites, *Cryst. Growth Des.*, 2006, **6**, 1717.

43 S. Gupta, Y. Batra, B. R. Mehta and V. R. Satsangi, Study of Charge Separation and Interface Formation in a Single Nanorod $CdS–Cu_xS$ Heterojunction Solar Cell using Kelvin Probe Force Microscopy, *Nanotechnology*, 2013, **24**, 255703.

44 F. Mesa, W. Chamorro, W. Vallejo, R. Baier, T. Dittrich, A. Grimm, M. C. Lux-Steiner and S. Sadewasser, Junction Formation of Cu_3BiS_3 Investigated by Kelvin Probe Force Microscopy and Surface Photovoltage Measurements, *J. Nanotechnol.*, 2012, **3**, 277.

45 J. Y. Kim, D. H. Youn, K. Kang and J. S. Lee, Highly Conformal Deposition of an Ultrathin FeOOH Layer on a Hematite Nanostructure for Efficient Solar Water Splitting, *Angew. Chem., Int. Ed.*, 2016, **55**, 10854.

46 R. Zhou and M. O. Guzman, CO_2 Reduction under Periodic Illumination of ZnS, *J. Phys. Chem. C*, 2014, **118**, 11649.

47 A. A. Bol and A. Meijerink, Luminescence Quantum Efficiency of Nanocrystalline $ZnS:Mn^{2+}$. 2. Enhancement by UV Irradiation, *J. Phys. Chem. B*, 2001, **105**, 10203; X. Wang, J. Shi, Z. Feng, M. Li and C. Li, Visible Emission

This journal is © the Partner Organisations 2020

Inorg. Chem. Front., 2020, **7**, 4687–4700 | **4699**

Characteristics from Different Defects of ZnS Nanocrystals, *Phys. Chem. Chem. Phys.*, 2011, **13**, 4715.

48 M. Ramya and S. Ganesan, Study of Thickness Dependent Characteristics of Cu_2S Thin Film for Various Applications, *Iran. J. Mater. Sci. Eng.*, 2011, **8**, 34.

49 S. Brunauer, L. S. Deming, W. E. Deming and E. Teller, On a Theory of the van der Waals Adsorption of Gases, *J. Am. Chem. Soc.*, 1940, **62**, 1723.

50 P. I. Ravikovitch, D. Wei, W. T. Chueh, G. L. Haller and A. V. Neimark, Evaluation of Pore Structure Parameters of MCM-41 Catalyst Supports and Catalysts by Means of Nitrogen and Argon Adsorption, *J. Phys. Chem. B*, 1997, **101**, 3671.

51 P. Kubelka, New contributions to the optics of intensely light-scattering materials: Part I, *J. Opt. Soc. Am.*, 1948, **38**, 448.

52 J. Tauc, Optical Properties of Amorphous Semiconductors, in *Amorphous and Liquid Semiconductors*, Plenum Press, New York, 1974, pp. 159–220.